Modeling of Direct Contact Condensation in the Water-Saturated Zone of the Soil Exposed to Steam Injection

Janfada, Taraneh Sadat; Kasiri, Norollah*[+]; Dehghani, Mohammad Reza

Computer-Aided Process Engineering (CAPE) Laboratory, School of Chemical, Petroleum & Gas Engineering, Iran University of Science and Technology, Tehran, I.R. IRAN

ABSTRACT: *In this research, the phenomenon of direct-contact condensation in porous media has been investigated based on the computational fluid dynamic technique, CFD, for hydraulic and thermal phenomena assessment. This phenomenon occurs in soil remediation by steam injection. The main contribution of this research is developing a new combined model for considering steam condensation in the saturated porous media systems using the direct contact condensation model, DCC, and Navier-Stockes equations rather than solely using Darcy's law-based model. For the first time, a two-resistance DCC model for porous media application has been included, predicting the propagation of steam front and condensation. The corresponding source and sink terms are due to the calculated condensation rate is added to each phase continuity equation and enthalpy equation of the liquid phase by user-defined functions, UDFs. Pressure drop due to flowing fluids in the porous structure was considered by lumped approach model using viscous and inertial loss terms added to momentum equations of the model. Heat loss from the sandbox is considered a sink term based on the calculated overall heat transfer coefficient and local temperature differences. The model results meet acceptable predictions for steam saturation content and temperature distributions over time and the predictions are qualitatively similar to the experimental and simulation results of the previous literature. The quantitative values of the sandbox-covered thermal areas were extracted from propagated saturated temperature fronts over processing time for both DCC simulation results and available experimental measurements, then the values were compared together. After elapsing 12 and 18 minutes from the beginning of the process, the simulation values of covered thermal areas are 0.049 m^2 and 0.082 m^2. The corresponding experimental values are 0.059 m^2 and 0.098 m^2, respectively. Evaluated absolute values of the relative change percent of covered thermal areas are 16.3% and 16.9% over processing times of 12 and 18 minutes.*

KEYWORDS: *Steam Injection; Remediation; Porous Media; Saturated Zone; Direct Contact Condensation; Modeling and Simulation; Computational Fluid Dynamic.*

***** *To whom correspondence should be addressed.*
+ *E-mail*: *capepub@cape.iust.ac.ir*
1021-9986/2022/3/1003-1021 19/$/6.09

INTRODUCTION

Over the last decades, the high risk of potable water being contaminated by polluted soil and also the potential of remedial actions on the soil unsaturated zone to prevent groundwater from being contaminated has been of high interest. Depending on the intensity and type of contaminants, all zones of soil containing unsaturated, groundwater level, and saturated zones may become polluted. Soil unsaturated zone, or vadose zone, is located below the land surface where the pores are not saturated with water. In contrast, the pores in the saturated zone are fully saturated with groundwater. The saturated zone is placed below the unsaturated zone. The zone between these two is referred to as the groundwater table.

Many different chemicals, physical, microbial, thermal, and plant-aid remediation techniques had been investigated for the removal of soil pollutants [1–5]. Steam injection technology is effectively applicable for the removal of immiscible volatile and semi-volatile contaminants from all zones. The steam injection can increase the vapor pressure of the volatile or semi-volatile components, hence speeding up the contaminant evaporation process and its eventual removal. The steam injection technique may also be used for the removal of Light Non-Aqueous Phase Liquids (LNAPLs) on the groundwater table. This method is particularly recommended for contaminates with large viscosity and low mobility placed on groundwater not readily and efficiently removable by a pump and treat methodology. Steam injection reduces viscosity and surface tension, thus increasing mobility and volatility and consequently speeding up contaminants removal [6]. Steam injection is also the proper methodology for remediation of Non-Aqueous Phase Liquids Denser than water (DNAPLs) located in the saturated zone. Although prevailing physical processes during steam injection into saturated and unsaturated zones are mainly the same, but there are still some distinct differences. One important difference in the saturated zone is the high effect of buoyancy force induced by the density difference of water and steam phases on steam propagation behavior. While in the unsaturated zone, the effect of the density difference between air and steam is not as much. In the soil-saturated zone, the density difference between steam, with a density of 0.554 kg/m^3, and liquid water, with 998.2 kg/m^3, is around 1500 times, which is much more than the density difference between steam and air with the air density being 1.225 kg/m^3 [7,8]. This physical parameter has a great influence on the configuration and propagation of the steam front in the saturated zone. Upward buoyancy forces compete with radial viscous forces resulting from pressure gradients induced by steam injection. Schematic figures for these forces and their directions are presented in Fig. 1. Depending on the ratio of these forces, if the viscose forces overcome the buoyancy forces, the steam area would have more propagation in the radial direction. Otherwise, steam moves more in the vertical direction and therefore does not have considerable progress inside the contaminated region [9,10].

Previously conducted research in the field can be categorized into steam injection in saturated and unsaturated zones. Emmert developed MUFTE simulator using a numerical model for nonisothermal gas-water systems in porous media [11]. *Helmig et al.* produced experimental data in one-dimensional unsaturated soil columns and reported moving condensation and drying fronts [12]. These were examined via steam, air, and hot air injection into the different saturated fine and coarse sand columns. Then the prediction ability of MUFTE simulator was checked by means of a comparison of well-controlled experiments and simulation results. Class et al. developed a complicated model to describe nonisothermal multiphase multicomponent physical systems in porous media with variable phase states [13]. In their model, an algorithm with adaptive switching of the primary variables according to the local phase states was implemented. Also, details of the physical and thermodynamic model conception, primary variable switching concept, and extended Multigrid method were described for the three-phase/three-component system, including water, NAPL, and gas phases. The model was then validated using the experimental data presented by *Class et al.* [14]. The experiments were conducted in an air-dry soil column of 30 cm in length and 10 cm in diameter contaminated by NAPL. This glass column is remediated using steam injection. The process front behavior was investigated and controlled by measuring temperatures using the sensors located 6.5, 14.5, and 23 cm from the top of the column [14]. Steam injection technology was improved using mixed air-steam co-injection based on the findings of *Schmidt et al.* [15]. They showed how pure steam injection might lead to severe downward migration. Similar experiments,

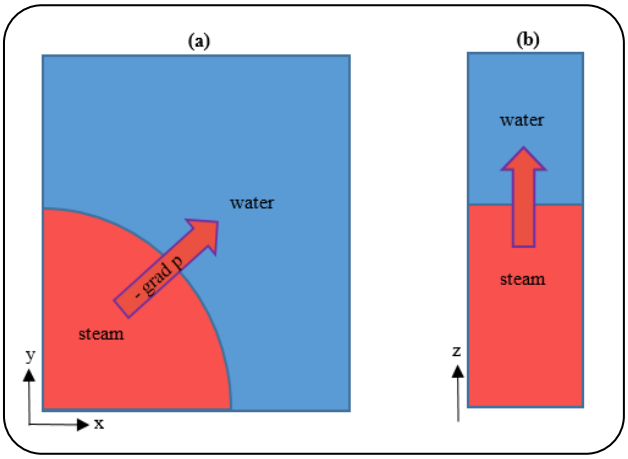

Fig. 1: (a) Radial viscous forces and advective flow induced by pressure gradients at the x-y plane view. (b) Vertical buoyancy forces and flow are induced by the density difference between water and injected steam in the z-direction view.

with simultaneous injection of steam and air, leading to no downward migration while rapid cleanup was still achieved. Two-dimensional experiments of steam injection into hydrocarbon-contaminated unsaturated porous media were performed. Similar experiments of steam and air mixture injection were also conducted. Gudbjerg carried out the simulation of pure steam injection and steam-air co-injection in the T2VOC software environment for the remediation of Mesitylene and DCB (1, 2-dichlorobenzene) in the unsaturated zone [16]. The simulation results were compared to the experimental data available in the research conducted by *Schmidt et al.* [15]. *Ochs et al.* investigated the steam injection process in the saturated zone using a two-dimensional sandbox [17]. One of the main parameters for the successful remediation of NAPL-polluted sites is the heating possibility of the polluted target region by delivering steam to the area. The experiments were performed to specify the extent of steam propagation and temperature distribution. *Ochs et al.* carried out their model based on an investigation in the saturated zone. This model has a variable degree of freedom due to the presence or absence of the phase resulting from condensation phenomena [17].

All of the above-mentioned simulation tools in the literature review, such as MUFTE and T2VOC, are component-based models. This means conservation equations are written for each component. Therefore, interfacial transport phenomena like condensation are implicitly considered in the component-based models and the conservation equations are inherently satisfied without the need to introduce condensation-related sink or source terms. Quite in contrast to the simulation tools introduced above, in the model presented here, the conservation equations are written for each phase. Therefore, interfacial mass transfer phenomena such as condensation are not considered implicitly. Thus, the model has to calculate the amount of condensed steam explicitly and then add it to the conservation equations of each phase as sink and/or source-related terms directly. In this approach, the required equations are extracted from the base models and the calculated amounts are then added as a source or sink terms to the mass conservation equations of each phase and the energy equation of the liquid phase. Although, apart from considering component-based or phase-based models for the phenomena, the physical basis is the same, when steam flows to a low-temperature region, to attain an equilibrium, part of the water component will transfer from the gas phase to the liquid phase. Since, in the same condition of 1 atm and 100°C, the specific enthalpy of liquid water, 417.51 kJ/kg, is less than that of vapor, 2675 kJ/kg, then along with condensation phase change, and in accordance with the energy conservation law, local temperatures would rise.

Direct contact condensation is occurring in soil water-saturated zone exposed to steam injection. Generally, direct contact condensation refers to vapor condensation in a liquid or condensation on liquid droplets entrained in the vapor [18]. The main objective of the work is the assessment of the effects and performance of saturated steam injection below the groundwater table in the saturated zone of the soil through the development of a Direct Contact Condensation model, DCC, within an Eulerian multiphase flow framework and a lumped approach treatment of the porous media involved. The main novelty of this research revolves around the combined use of the Eulerian approach with the inclusion of the Navier Stokes equation besides Darcy's law and DCC for the first time to model condensation during steam injection within the porous media. In none of the previous works, the DCC model had not been used for porous media systems. Also, quite contrary to all previous efforts in the field of steam injection, which have used solely simplified Darcy's law approach and therefore have accuracy limitations, in this research, Navier-Stokes equations are used in addition to Darcy's law equation. This computational fluid dynamic

technique can enable for having a more accurate estimation of a heating pattern of steam injection and condensation rate below the groundwater table in the saturated zone of the soil.

In this paper, new functions of direct contact condensation and lumped approach porous media models have to be defined and added using UDFs to the Eulerian-based model. In this research, steam condensation rate, temperature, water saturation distributions, and propagation of heat front are investigated and compared with the available experimental and simulation results. As a result of the current work the heat front propagation is to be predicted in the water-saturated zone of the porous soil and this would enable one to predict the time and condition in which the steam reached the targeted and presumed contaminated zone.

THEORETICAL SECTION

Mathematical modeling and methods

Considering the very low saturation availability of the contaminate phase in the system and therefore have the negligible effect of contamination on steam propagation, thermal front, and hydraulic, then it is possible to model the system by only including water and steam phases and ignoring the contamination phase. This enables to have uncomplicated hydraulic analysis for steam propagation, which is the objective of the current work. Therefore, the model developed in this paper does not contain the contaminant component. In order to carry out remediation scenarios, it would only be required to include the contaminant component.

In this study, the steam injection process is simulated using the Eulerian multiphase flow model combined with Darcy's law equation and DCC model, for the flume filled with sand and saturated with water.

The steam injection model based on DCC consists of three sub-models,

1- Eulerian multiphase flow model
2- Direct contact condensation model
3- Lumped approach porous media model

Eulerian multiphase flow model

The pressure and velocity fields of phases during the steam injection process is calculated with the Eulerian multiphase flow model. This considers volume fraction, mass, momentum, and energy conservation equations for each phase individually [19,20]. The volume of q^{th} phase, V_q, is defined by;

$$V_q = \int_V \alpha_q \, dV \tag{1}$$

In which α_q and V are representative of the volume fraction of the q^{th} phase and total volume. The total summation of all volume fractions of phases is equal to unity, thus;

$$\sum_{q=1}^{n} \alpha_q = 1 \tag{2}$$

A mass balance on the q^{th} phase gives a continuity equation of the phase q;

$$\frac{\partial(\alpha_q \rho_q)}{\partial t} + \nabla . (\alpha_q \rho_q \mathbf{u}_q) = \sum_{p=1}^{m} (\dot{m}_{pq} - \dot{m}_{qp}) + S_q \tag{3}$$

The first and second terms on the left-hand side of the mass conservation equation is related to unsteady terms of mass accumulation and the contribution of mass advection, respectively. In which, $\mathbf{u}_q$ is the q^{th} phase velocity, and ρ_q is an indicator of the q^{th} phase density. The first term on the right-hand side of Eq. (3) is the source term due to mass transfer regarding phase change, like condensation or evaporation. In this way, the summation $\dot{m}_{pq}$ indicates the sum of mass transferred from all p phases to the q^{th} phase. Inversely, the summation $\dot{m}_{qp}$ is the sum of mass transferred from the q^{th} phase to all p phases. Also, S_q is representative of other source/sink terms [21,22].

Writing a momentum balance on each phase gives a momentum conservation equation for each phase; here for the q^{th} phase;

$$\frac{\partial}{\partial t}(\alpha_q \rho_q \mathbf{u}_q) + \nabla . (\alpha_q \rho_q \mathbf{u}_q \mathbf{u}_q) = \tag{4}$$

$$-\alpha_q \nabla P + \alpha_q \rho_q \mathbf{g} + \nabla . \bar{\bar{\boldsymbol{\tau}}}_q +$$

$$\sum_{p=1}^{n} (\mathbf{R}_{pq} + \dot{m}_{pq} \mathbf{u}_{pq} - \dot{m}_{qp} \mathbf{u}_{qp}) + (\mathbf{F}_q + \mathbf{F}_{lift,q} + \mathbf{F}_{vm,q})$$

The first term on the left-hand side of Eq. (4) is momentum accumulation, and the second term is related to the contribution of momentum advection. The first three terms on the right-hand side of Eq. (4) represent pressure force, gravitational, and shear stress forces. In this part, P

presents the distributed pressure for all phases and $\bar{\bar{\tau}}_q$ is the stress-strain tensor of the q^{th} phase. In the fourth right-hand side expression of Eq. (4), $\mathbf{R}_{pq}$ is an interaction force between phases. Also, in this part, the summation of $\dot{m}_{pq}\mathbf{u}_{pq}$ indicates the sum of the momentum transferred from all p phases to the q^{th} phase. Inversely, the summation of $\dot{m}_{qp}\mathbf{u}_{qp}$ is the sum of the momentum transferred from q^{th} phase to all p phases, in which $\mathbf{u}_{pq}$ and $\mathbf{u}_{qp}$ are the interphase velocities. Afterward, $\mathbf{F}_q$ represents the external body force, including buoyancy, $\mathbf{F}_{lift,q}$ is lift force, and $\mathbf{F}_{vm,q}$ is representative of virtual mass forces.

Separate enthalpy equations for each phase are used to describe the conservation of energy in the multiphase model. Hence for phase q;

$$\frac{\partial}{\partial t}(\alpha_q \rho_q h_q) + \nabla.(\alpha_q \rho_q \mathbf{u}_q h_q) = \tag{5}$$

$$-\alpha_q \frac{\partial p_q}{\partial t} + \bar{\bar{\tau}}_q : \nabla \mathbf{u}_q - \nabla.(k_{cond-q} \nabla . T_q)$$

$$+ \sum_{p=1}^{n} (Q_{pq} + \dot{m}_{pq} H_{pq} - \dot{m}_{pq} H_{pq}) + S_q$$

The first and second terms on the left-hand side of the energy conservation equation are the unsteady term related to enthalpy accumulation and the contribution of enthalpy advection, respectively. In which $\boldsymbol{u}_q$ is the q^{th} phase velocity, and h_q denotes the specific enthalpy of the q^{th} phase. The first right-hand side term of Eq. (5) is representative of the energy related to the pressure presence. The second term is the dissipation term related to shear stress. The third term represents the inner heat conduction of q^{th} phase. The summation term of Q_{pq} is the sum of the heat exchange intensity between the q^{th} and other phases. It is assumed that the rate of interfacial heat transfer between phases is a function of the temperature difference and the interfacial area, A_i;

$$Q_{pq} = h_{pq} A_i (T_p - T_q) \tag{6}$$

where h_{pq} is the heat transfer coefficient between the p^{th} and the q^{th} phases depending on the p^{th} phase Nusselt number (Nu_p), by;

$$h_{pq} = \frac{k_{cond-q}\, Nu_p}{d_p} \tag{7}$$

In which, k_{cond-q} is the thermal conductivity coefficient of the q^{th} phase and d_p is the bubble diameter of the p^{th} phase [21,23]. In the case of fluid-fluid multiphase flow systems, the Nusselt number can be calculated using the Ranz-Marshall correlation [24]. The summation term of $\dot{m}_{pq}H_{pq}$ in Eq. (5) indicates the sum of energy transferred from all p phases to the q^{th} phase, and inversely, the summation term of $\dot{m}_{pq}H_{pq}$ indicates the sum of the energy transferred from the q^{th} phase to all p phases. H_{pq} denotes the interphase enthalpy. Also, S_q is the indicator for other enthalpy sources like chemical reactions or radiation sources, which are not included in the steam injection process [21,22].

Although these equations are written here only for phase q, in an Eulerian framework, similar equations ought to be written and discretized for all other available phases. Assuming low saturation of the contaminant phase and therefore, having a negligible effect on the contaminant on steam propagation, it is possible to ignore the contaminant phase. Therefore, only conservation equations are considered for the water and steam phases.

Direct contact condensation model

In a direct contact condensation model, the condensation phenomenon is considered a result of direct contact with steam and water. DCC model considers thermal equilibrium on the interfacial area of available liquid and vapor phases in each computational cell. Therefore, the interfacial area between two phases in each cell is considered to be in the saturated condition. The saturation temperature of the interfacial area in each cell is calculated using the Antoine equation at local cell pressure. A schematic plot of mass and heat transfer from the gas phase into the interfacial area and from there to the liquid phase in each cell is shown in Fig. 2. In a DDC model, the heat transfer process is considered separately for liquid and vapor phases. In other words, the model is a two-resistance model, in which the heat transfer process on both sides of the interfacial contact area separately accounted for the water and steam phases in each cell. Heat flux from the interface to the liquid side is set equal to heat flux from the vapor side to the interface leading to the calculation of the condensation rate. Then, the source terms due to the calculated condensation rate are added to the energy conservation equation of the liquid phase and continuity equations of each used phase in the multiphase flow model. Mass and energy transfer rates during direct contact condensation of vapor and water are defined based on three important parameters:

interfacial area, interfacial heat transfer coefficient, and interfacial mass transfer. These parameters are described below.

Interfacial mass transfer

Since there is no predefined model for direct contact condensation in FLUENT, the elements of the condensation model have to be defined as user-defined functions. The mentioned user-defined functions enable the source or sink terms based on the DCC model to be added to the continuity equations of each phase and the energy conservation equation of the liquid phase.

The rate of condensed mass passing through the gas phase to the interface is equal to the rate of the mass passing through the interface to the liquid phase. The interfacial mass transfer could be calculated by total heat balance [25,26]. The net of inlet and outlet heat flux passed from the interface is equal to zero as the interface is under equilibrium conditions.

$$Q_{gas-int} + Q_{int-liq} = 0 \quad (8)$$

Thus, the two heat flow rates are equal;

$$Q_{int-liq} = - Q_{gas-int} \quad (9)$$

Which, $Q_{gas\text{-}int}$ represents heat transfer from the vapor to the interfacial area and $Q_{int\text{-}liq}$ shows heat transfer from the interfacial area to the liquid phase. Using Eq. (9), it is possible to calculate the rate of interfacial mass transfer. Heat flux from the steam side to the interfacial area, $Q_{gas\text{-}int}$, being the heat loss during steam condensation, is given by;

$$Q_{gas-int} = q_g + \dot{m}_{gas\_int} H_{gs} \quad (10)$$

The first term of Eq. (10), q_g, is steam phase convective heat transfer and depends on the temperature difference between gas and interfacial area. This term could be calculated by Eq. (11);

$$q_g = h_g (T_g - T_{int}) \quad (11)$$

in which, h_g is the vapor phase convective heat transfer coefficient, T_g is the temperature of gas-phase, and T_{int} is interfacial temperature, assumed to be saturation temperature at local pressure.

The second term in Eq. (10) represents the amount of enthalpy transfer due to condensation, in which $\dot{m}_{gas\text{-}int}$ is the rate of the mass transfer from the gas phase to the interface, and H_{gs} is the saturation enthalpy of the gas phase. In fact, the enthalpy reduction of the gas phase depends on the condensation rate.

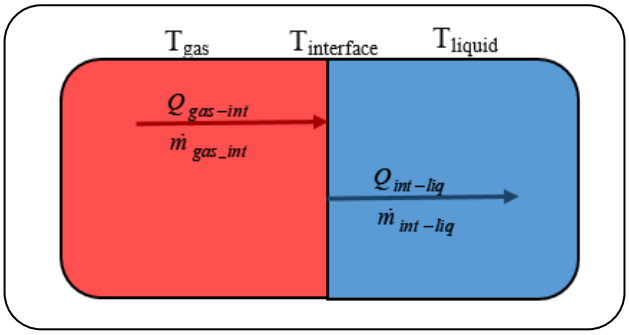

Fig. 2: Schematic plot of mass and heat transfer from the gas phase into the interfacial area and from there to the liquid phase in each cell

Heat flux from the interfacial area to the liquid phase, $Q_{int\text{-}liq}$, is given by;

$$Q_{int-liq} = q_l + \dot{m}_{int-liq} H_{ls} \quad (12)$$

The first term on the right-hand side, q_l, is liquid phase convective heat transfer and depends on the temperature difference between interface and liquid and can be calculated by Eq. (13), in which h_l is liquid phase convective heat transfer coefficient.

$$q_l = h_l (T_{int} - T_l) \quad (13)$$

The second term in Eq. (12) represents the enthalpy transfer due to condensation mass transfer, $\dot{m}_{int\text{-}liq}$ is the mass flow rate of the condensate, passing through the interface to the liquid phase, and H_{ls} is the saturation enthalpy of the liquid phase. Indeed, the enthalpy increment in the liquid phase depends on the condensation rate. The condensate transfers energy during the mass transfer from the gas phase to the liquid phase.

The net value of inlet and outlet mass flow rates passed from the interface is equal to zero. In other words, the two mass flow rates are equal;

$$\dot{m}_{int-liq} = -\dot{m}_{gas-int} \quad (14)$$

Eq. (12) can be rewritten using Eq. (14), as;

$$Q_{int-liq} = q_l + (-\dot{m}_{gas-int}) H_{ls} \quad (15)$$

Substituting this and Eq. (10), in the overall heat balance of Eq. (9), gives;

$$q_l - \dot{m}_{gas-int} H_{ls} = -(q_g + \dot{m}_{gas-int} H_{gs}) \quad (16)$$

The mass transfer rate from the gas phase to the interface, $\dot{m}_{gas-int}$ (kg/m^3s), can be extracted from Eq. (16) as;

$$\dot{m}_{gas-int} = -(q_l + q_g)/(H_{gs} - H_{ls}) \quad (17)$$

Thus, the mass transfer rate to the liquid phase may be obtained by;

$$\dot{m}_{int-liq} = (q_l + q_g)/(H_{gs} - H_{ls}) \quad (18)$$

The denominator term of Equations (17) and (18) is the latent heat of evaporation. Tortike and Farouq's equation may be used to evaluate it based on the variable of T_s (K), saturation temperature [27];

$$\Delta H_{evap} = (7184500 + 11048.6\, T_s - 88.4050\, T_s^2 + 0.162561\, T_s^3 - 1.21377\times10^{-4} T_s^4)^{1/2} \quad (19)$$

Absolute output values of $\dot{m}_{gas-int}$ and $\dot{m}_{int-liq}$, calculated with UDFs, are equal together. However, these two flow rates have opposite signs. In fact, $\dot{m}_{gas-int}$ is negative, since mass is leaving the gas phase, and $\dot{m}_{int-liq}$ is positive because mass is gaining on the liquid side. Also, $Q_{gas-int}$ is negative since heat is leaving the gas phase, and $Q_{int-liq}$ is positive because heat is gaining on the liquid side. Condensation rates for all the computational cells are calculated and compiled to the model by using DEFINE_SOURCE (src_con_liq,c,fir_th,dS,eqn) and DEFINE_SOURCE (src_con_gas,c,sec_th,dS,eqn) Macros. In addition, the liquid energy source term for each cell, which is containing the sum of $\dot{m}_{int-liq} H_{ls}$ and $\dot{m}_{int-liq} \Delta H_{evap}$, can be compiled to the model by DEFINE_SOURCE (src_energy_liq,c,fir_th,dS,eqn) Macro.

Interfacial area

The determination of the volumetric heat transfer coefficient requires an estimation of interfacial area per unit volume (A_{lg}), which can be estimated by the Symmetric Model. In this model, the interfacial area concentration approaches zero when α_g approaches one.

$$A_{lg} = \frac{6\alpha_g(1-\alpha_g)}{d_g} \quad (20)$$

Heat transfer coefficients of liquid and steam phases

As it is assumed in the two-resistance DCC model, heat transfer accomplishes over two stages, from vapor to interface and from there to liquid. Therefore, it is necessary to evaluate heat transfer coefficients for each phase separately. This model applies the liquid heat transfer coefficient, h_l, calculated by Nusselt number Ranz-Marshall correlation, for each cell containing gas and liquid phases along with required modifications using logical and real physical assumptions. Volumetric heat transfer coefficient for liquid phase, H_l (W/m^3K), using interfacial area is given by;

$$H_l = h_l A_{lg} \quad (21)$$

The following constant value is implemented for the heat transfer coefficient of the vapor phase. *Brucker* and *Sparrow* suggested this value based on assuming that the steam temperature is close to the saturation temperature.

$$h_g = 10^4 \quad W/m^2K \quad (22)$$

The volumetric heat transfer coefficient for gas phase, H_g (W/m^3K), is to be calculated using the following equation [28].

$$H_g = h_g A_{lg} \alpha_l \quad (23)$$

In the case of no existence of direct contact between steam and water in any computational cell due to the non-availability of one of the phases, the direct contact condensation phenomenon is not occurring in that cell. Due to this reality, employing the volume fraction of the liquid phase and interfacial area in Eq. (23), the volumetric heat transfer coefficient for the gas phase can be enforced to be zero in the cells containing just one of the liquid/steam phases.

Porous media model

In this paper, Lumped Parameters approach is used to model the porous media of the sandbox. In this approach, all phases, excluding the solid phase, are considered as a phase in the model formulation, and the volume fraction of each phase in each cell is calculated based on the porous media void fraction, which is called porosity.

The physical property of hydraulic conductivity, with the dimensions of length per time (L/T), measures

the ability of the material to transmit fluid through pore spaces in the presence of an applied hydraulic gradient. Hydraulic conductivity depends on both properties of the porous medium (intrinsic permeability) and the fluid flowing through it, consisting of the degree of saturation, the density, and the viscosity of the fluid. As different fluids in the same porous media could have different hydraulic conductivities, therefore, in order to use the acquired hydraulic conductivity for other fluids, the properties of porous media have to be separated from the properties of the fluid by applying intrinsic permeability. This parameter, which is also called specific permeability or absolute permeability and is shown by *k*, has the dimension of length squared (L^2) and only consists of porous media properties like particle shape, size, diameter, packing, and interconnectedness of the pores. Symbolically the separation of hydraulic conductivity, *K*, into two distinct contributions owing to the structure of the porous matrix, *k*, and the properties of the fluid containing density, ρ, and viscosity, μ, is presented below [29];

$$K = k\frac{\rho g}{\mu} \tag{24}$$

Conversely, absolute permeability can be calculated by;

$$k = K\frac{\mu}{\rho g} \tag{25}$$

If hydraulic conductivity is to be extracted by water liquid flow experiment, then for calculating the absolute permeability, the density and viscosity of the liquid water have to be substituted in Eq. (25) instead of ρ and μ.

Absolute permeability is defined merely for a single-phase system. Although, porous media systems commonly contain two or more fluids. Hence, effective permeability, k_i, which is a saturation-based function, has developed for multiphase flows in porous media. Effective permeability is representative of the potential of a porous medium for being saturated with each of the available fluids in the system. The ratio between effective permeability and absolute permeability is defined as a dimensionless parameter of relative permeability, k_{ri} [29].

$$k_{ri} = \frac{k_i}{k} \tag{26}$$

In a porous media two-phase flow system, the wetting phase is the phase with more tendency to spread on the solid compared to the other immiscible phase of the system. Non-wetting phase has less tendency to spread on the solid [29]. Relative permeability for wetting (*w*) and non-wetting (*n*) phases, which are respectively liquid water and vapor in this paper, can be calculated by Van Genuchten correlations are presented in Eq. (27) and Eq. (28). The range of relative permeability is between zero and one. It shows the ability of a system for flowing one fluid in the presence of another fluid for a two-phase flow in porous media systems [30].

$$k_{rw}\left(S_w\right) = \left(S_{we}\right)^{1/2}\left(1-\left(1-S_{we}^{\frac{n}{n-1}}\right)^{\frac{n-1}{n}}\right)^2 \tag{27}$$

$$k_{rn}\left(S_n\right) = \left(S_{ne}\right)^{1/3}\left(1-\left(1-S_{ne}\right)^{\frac{n}{n-1}}\right)^{\frac{2(n-1)}{n}} \tag{28}$$

In the above correlations, *n* is the Van Genuchten parameter. The effective saturation of wetting and non-wetting phases, S_{we} and S_{ne}, also can be computed based on residual saturation of wetting and non-wetting phases, S_{wr} and S_{nr}, as defined by [30];

$$S_{we} = \frac{S_w - S_{wr}}{1-\left(S_{wr}+S_{nr}\right)} \tag{29}$$

$$S_{ne} = \frac{S_n - S_{nr}}{1-\left(S_{wr}-S_{nr}\right)} \tag{30}$$

In the current porous media model, the pressure gradient for each phase is calculated by a momentum sink, which is proportional to the fluid velocity of each cell as follows [21];

$$sink_{(i)} = -\left(\frac{\mu}{k_i}\mathbf{u}_i + C_i\frac{1}{2}\rho\left|\mathbf{u}_i\right|\mathbf{u}_i\right) \tag{31}$$

The right-hand side of Eq. (31) is composed of two parts, the first term is the viscous loss term, and the second term is the inertial loss term. The viscous loss term plays a more important role compared to the inertial loss term in the modeling of laminar flows having low Reynolds numbers. Mostly, the laminar regime is governing in steam injection flows for soil remediation purposes. The inertial loss represents the kinetic energy related to the dynamic head,

and it is more important at high Reynolds numbers. In Eq. (31), C_i is the inertial resistance parameter for phase i and k_i is effective permeability, extracted from Eq. (25) and Eq. (26);

$$k_i = k_{ri} k = k_{ri} K \frac{\mu}{\rho g} \tag{32}$$

Indeed, the first term of Eq. (31) is equal to Darcy's equation for multiphase flows [13,31]. In which, pressure drop depends on velocity, and can be written for the wetting phase as;

$$\nabla p_w = -\frac{\mu_w}{k_w} u_w \tag{33}$$

Effective permeability of the wetting phase, k_w, can be calculated using Eq. (32);

$$k_w = k_{rw} k \tag{34}$$

For the non-wetting phase, Darcy's equation can be written as;

$$\nabla p_n = -\frac{\mu_n}{k_n} u_n \tag{35}$$

k_n can be calculated using;

$$k_n = k_{rn} k \tag{36}$$

In Eq. (34) and Eq. (36), relative permeabilities of k_{rw} and k_{rn} can be calculated using Eq. (27) and Eq. (28), and the experimental value of absolute permeability, $k\ [L^2]$, is reported in Table 1.

The second term in Eq. (31), the inertial loss term, has a minor effect on calculated pressure drop values in laminar flows, although it has to be considered for higher Reynolds numbers. For the first time, in 1901, *Forchheimer* showed that deviation of Darcy's law predictions from measurements could be highly related to the kinetic effect of the fluid and dynamic head in high Reynolds numbers. Therefore, Darcy's law equation was modified for non-laminar flows by adding kinetic energy term, as [31];

$$\nabla p = -\left(\frac{\mu}{k} \mathbf{u} + a \rho |\mathbf{u}| \mathbf{u} \right) \tag{37}$$

in which a is the Forchheimer constant and k is the intrinsic permeability. The following equation is proposed for which C_E is the Ergun constant [31];

$$a = C_E / k^{1/2} \tag{38}$$

Eq. (37) can be expressed individually for each phase in multiphase flow systems. For the i^{th} phase it is written as;

$$\nabla p_i = -\left(\frac{\mu_i}{k_i} \mathbf{u}_i + a_i \rho_i |\mathbf{u}_i| \mathbf{u}_i \right) \tag{39}$$

For each phase of multiphase flow, Eq. (38) may be written as;

$$a_i = C_E / k_i^{1/2} \tag{40}$$

Thus, C_i could be evaluated by equating the right-hand sides of Eq. (39) and Eq. (31) and also substituting Eq. (40) instead of a_i;

$$C_i = 2 a_i = 2 C_E / k_i^{1/2} \tag{41}$$

Dimensionless parameter of Ergun constant, C_E, varies with porosity and porous media structure variations and may be computed as follows [21];

$$C_E = \frac{1.75}{d_m} \frac{(1-\varepsilon)}{\varepsilon^3} \tag{42}$$

in which, ε is the porosity and d_m is the mean bed particle diameter. Therefore, Eq.(41) may be rewritten using Eq. (42), as;

$$C_i = 3.5\, k_i^{-1/2} \frac{(1-\varepsilon)}{\varepsilon^3} \frac{1}{d_m} \tag{43}$$

The following equations are presented for evaluation of the inertial resistance parameters of the wetting and the non-wetting phases of a two-phase flow system;

$$C_w = 3.5\, k_w^{-1/2} \frac{(1-\varepsilon)}{\varepsilon^3} \frac{1}{d_m} \tag{44}$$

$$C_n = 3.5\, k_n^{-1/2} \frac{(1-\varepsilon)}{\varepsilon^3} \frac{1}{d_m} \tag{45}$$

Effective permeabilities of k_n and k_w are defined in Eq. (34) and Eq. (36).

Viscous and inertial loss parameters are defined in the UDF by DEFINE_ ADJUST (porous_data, domain) Macro, using the Equations of (27-30, 34, 36, 44-45). Then in the cell zone conditions part of the ANSYS

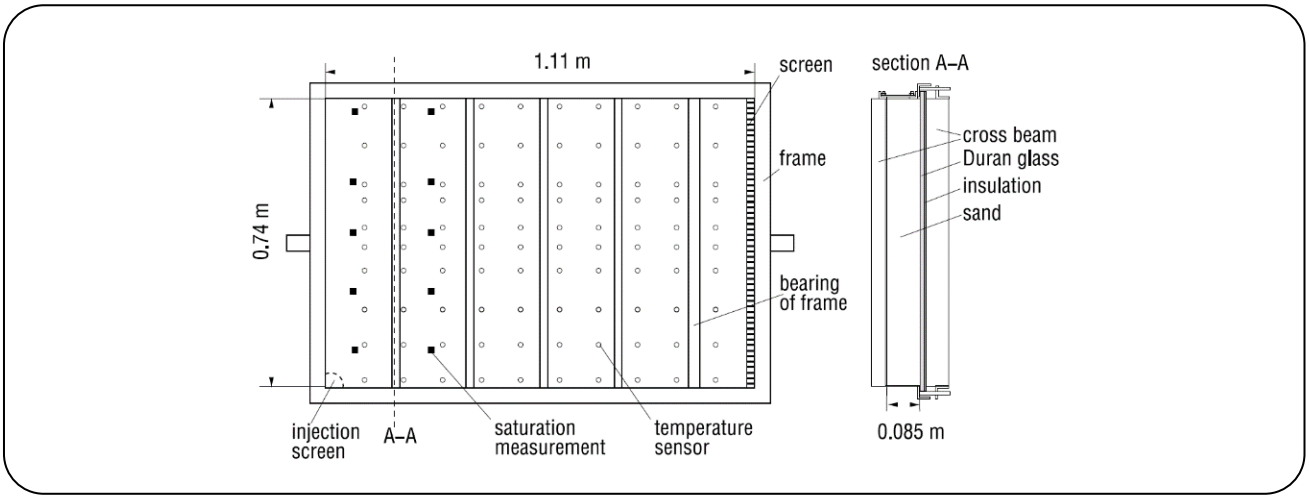

Fig. 3: Schematic of the experimental setup for steam injection tests in the saturated zone, "Reprinted with permission from Ref. [17]. Copyright 2010 by the American Geophysical Union."

simulator, the computed porous zone parameters are inserted and to be compiled by the written DEFINE_PROFILE Macros in the UDF.

Simulation of steam injection in the water-saturated sandbox

Modeling and simulation of steam injection in a fully water-saturated zone of porous media is accomplished, and the results are validated against available simulation and experimental data of VEGAS (Versuchseinrichtung zur Grundwasser und Altlastensanierungull), Research Facility for Subsurface Remediation at Stuttgart University. The used experimental setup consists of a sandbox with a height of 0.74 m, a length of 1.1 m, and a width of 0.085m. In this research, for modeling the setup, a two-dimensional model is considered due to the low width of the sandbox. the layout of the experimental setup is shown in Fig. 3.

Based on the physical conditions of the setup boundaries, no-flow wall Neumann boundary conditions are defined at all walls of the flume, except for the two boundaries, as displayed in Fig. 4. The mass inflow boundary condition is employed in the inlet port of the sandbox, shown in the left-hand side of Fig. 4. This boundary condition represents the steam injection mass flow rate into the domain at the fixed value of 0.001 kg/s, equal to 3.6 kg/h. The outlet port, on the middle right-hand side of the flume, is modeled using pressure outlet boundary condition.

Considering the mesh independence study, the total number of 32856 square quadrilateral cells are

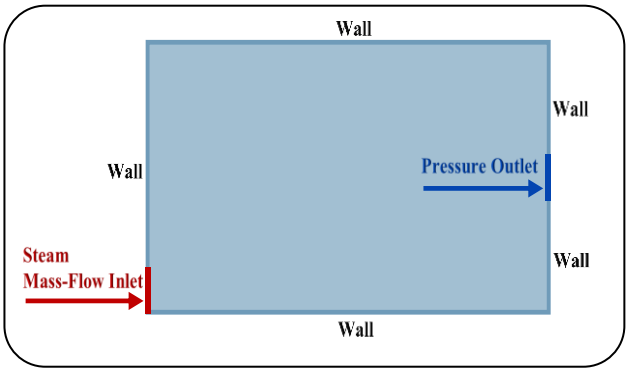

Fig. 4: The boundary conditions of the sandbox under soil water-saturated conditions with a steam flow velocity of 3.6 kg/h.

implemented for the computational model. The system is initially to prevail under ambient temperature conditions of 298.15K, and the water volume fraction set is equal to one. Required parameters for the simulation of a two-phase flow system of water and vapor in the sand porous media are stated in Table 1.

Multiphase Eulerian Coupled Algorithm is used for solving the pressure and velocity field of the two phases as well as solving the heat equation. The laminar Flow model is used due to the low velocity and low calculated values of the Reynolds number based on the hydraulic diameter of the steam inlet port, also based on Reynolds number calculation in porous media. A symmetric model is used for Drag function evaluation. The heat transfer coefficient between the two phases is calculated using Ranz-Marshal correlation. The saturation temperature in each cell is calculated using the Antoine equation at local cell pressure in the UDF.

Table 1: Sand properties and specifications, "Reprinted with permission from Ref. [17]. Copyright 2010 by the American Geophysical Union."

Sand Properties	Symbol [unit]	Value
Porosity	ε [-]	0.34
Absolute permeability	k [m^2]	6.63×10^{-11}
Van Genuchten parameter, n	n [-]	7.4
Van Genuchten parameter, α_{VG}	α_{VG} [Pa^{-1}]	6×10^{-4}
Residual water saturation	S_{wr} [-]	0.12
Residual gas saturation	S_{nr} [-]	0.0
Soil grain density	ρ_{sg}[$kg.m^{-3}$]	2650
Specific heat capacity of soil	c_{pm} [kJ/(kg.K)]	850
Thermal conductivity of dry soil	k_s [W/m K)]	0.582

The first-order Upwind schemes are used for the discretization of convective terms in the momentum equations, and energy equations, and also for volume fraction discretization. Water liquid and vapor properties such as density, viscosity, thermal conductivity, and specific heat capacity are derived using ANSYS material database. In addition, a solid database of steel and silica is used for the soil grains and the metal in the sandbox apparatus.

RESULTS AND DISCUSSIONS

The following have resulted from the DCC model in porous media incorporated into the simulation of injecting saturated steam within the fully water-saturated sandbox. Temperature and liquid-water saturation distributions are displayed in Fig. 5 and Fig. 6 during steam injection in the sandbox under soil water-saturated conditions with the steam flow velocity of 3.6 kg/h, over processing times of 6, 12, and 18 minutes. On the extreme right and the left side of the flume, 6.5 cm from the end, a mesh screen is used over the full height of the sandbox to separate the porous section from the injection and extraction chambers. Therefore, all simulation and experimental map plots in Fig. 5 and Fig. 6 show merely the predictions and available measurement values of the porous section, with a 6.5 cm distance from the right wall of the flume. Although, the x-axis of all figures started from zero.

Simulation results of the DCC model in the porous media for liquid-water saturation distribution are shown in Figs. 5(a-c) and are compared qualitatively to Figs. 5(d-f) and Figs. 5(g-i), which are numerical results of Darcy's law-based model and experimental γ- density measurements reported by *Ochs et al.* [17]. As expected, the values of liquid-water saturation within the vicinity of the steam injection area are close to zero. In other words, steam saturation within the vicinity of the steam injection area is close to unity. The values of liquid water and steam saturation in the foreside of the steam propagation front are close to one and zero, respectively. Between the progressive steam front and the injection area, the values of liquid-water saturation are between zero to one, and conversely, the values of steam saturation are between one to zero.

As it is evident from Fig. 5, the spreading behavior and the shape of the fronts can be reproduced with the DCC model. Simulation results of the DCC model in porous media agree with and match the previous experimental and simulation results. The simulation results of the DCC model, despite slight deviations from the experimental measurements, agree very well with Darcy's law-based model results. The mentioned deviations can be due to the two reasons are explained below.

The first one can be related to the real experimental conditions with having no entirely pure steam in the process. Indeed, the used steam in the experiment might consist of some small volumes of air gases, the same dissolved gases of liquid water, which are released from the liquid during steam generation and transferred along with steam into the sandbox. As the water vapor component is condensable, it would be condensed when encountering areas having lower temperatures than the saturated steam. Any possible available non-condensable

gases can go more forward into the porous medium. This movement propagates into the system as far as air gas entrapment occurs between the pores. This entrapment happens a little farther away from the condensation front. Therefore, a wider spread of the propagated area, containing water-liquid saturations with values less than one, could be resulted in the available experimental measurements compared to simulation results.

Based on the experimental report of Ochs et al., another important reason for the mentioned deviation is regarding the sequential procedure of measurements by the γ density measurement device with approximately every 30 seconds for completing each required sequence. Thus, during a sequence of measurements, progressing front eventually arrives at a position, where there were fully liquid-water saturated conditions at the beginning [17]. For instance, the measured water saturation after 6 minutes in Fig. 5g shows an experimental value of about 0.5 at the point of (0.0m, 0.3m). While, at the same point, the simulation results of Fig. 5a still indicate fully saturated conditions (S_w = 1.0). At the same time, the DCC simulation result of the liquid-water saturation is about 0.5 at the point of (0.0m, 0.21m).

Temperature distribution results of the porous media DCC model are shown in Fig. 6(a-c). Using Figs. 6(d-f), 6(g-i), and 6(j-l), DCC model temperature distributions are qualitatively compared to Darcy's law-based model results, experimental temperature measurements of Pt-100 sensors, and thermographic camera, which have been reported by *Ochs et al*. [17].

As expected, the values of temperature within the vicinity of the steam injection area are close to the saturated steam temperature of 373.15K. Temperature values beyond the thermal front are equal to the initial temperature of the porous media, ie 298.15K. Between the progressive thermal front and the injection area, temperature values are between 373.15K and 298.15K. Using Fig. 6, it is evident that the simulation results of the DCC model in porous media demonstrate a very good agreement with Darcy's law-based model results. The spreading behavior and the shape of the fronts can be reproduced, but the simulation results of the DCC and Darcy's law-based models show some deviations from the experimental measurements. The deviations can be the consequence of some available physical circumstances in the experiments, as explained in the following.

Experimental temperature distributions in Figs. 6(g-i) were derived using Pt-100 temperature sensors, which are arranged at a 10cm distance from each other. Therefore, the saturated front can merely be recognized when the front reaches the sensors. Thus, linear interpolation on such coarse spatial resolution is accompanied by some inaccuracy in the plotted experimental steam fronts extracted from Pt-100 temperature sensors. In particular, this inaccuracy is more at saturated fronts due to the steep temperature gradient between the condensate and steam boundary. Thus, one of the reasons for available differences between the pt-100 experimental measurements and simulation results can be related to experimental inaccuracies. On the other hand, DCC and Darcy's based law models predict a slightly larger horizontal extension of the steam zone than what is shown by the measurements. This can be related to the high heat conductivity of the used steel framework and, therefore, higher heat losses from there.

The main reason for having deviations between the experimental thermographic camera measurements, Figs. 6(j-l), and simulation results are related to removing insulation to take photos with the thermographic camera, which causes higher heat losses to the environment thus observing less propagated areas during measuring times. Again, another reason is related to the used steel framework and metal beams, which are utilized for holding together the apparatus and surrounding the glass part of the experimental setup. Temperature measurements with the thermographic camera shows lower temperatures, especially near the bottom framework boundary of the sandbox and also when the propagated thermal front reaches the metal beams. This is due to higher heat losses regarding higher thermal conductivities of the steel framework at the bottom of the sandbox and metal beams. This issue causes obvious vertical breakdowns and disconnections in the temperature distributions, which can be seen in Fig. 6(j-l). The mentioned reasons related to heat losses are not available and thus effective in the process of steam injection at real contaminated sites. In addition, the simulation of steam injection is very complex and considering all sandbox physical details in the model is not reasonable and feasible. Therefore, in order to simplify and reduce computational costs one may consider heat losses as a sink term. In this case, the sink term to be calculated based on the computed overall heat transfer coefficient and local

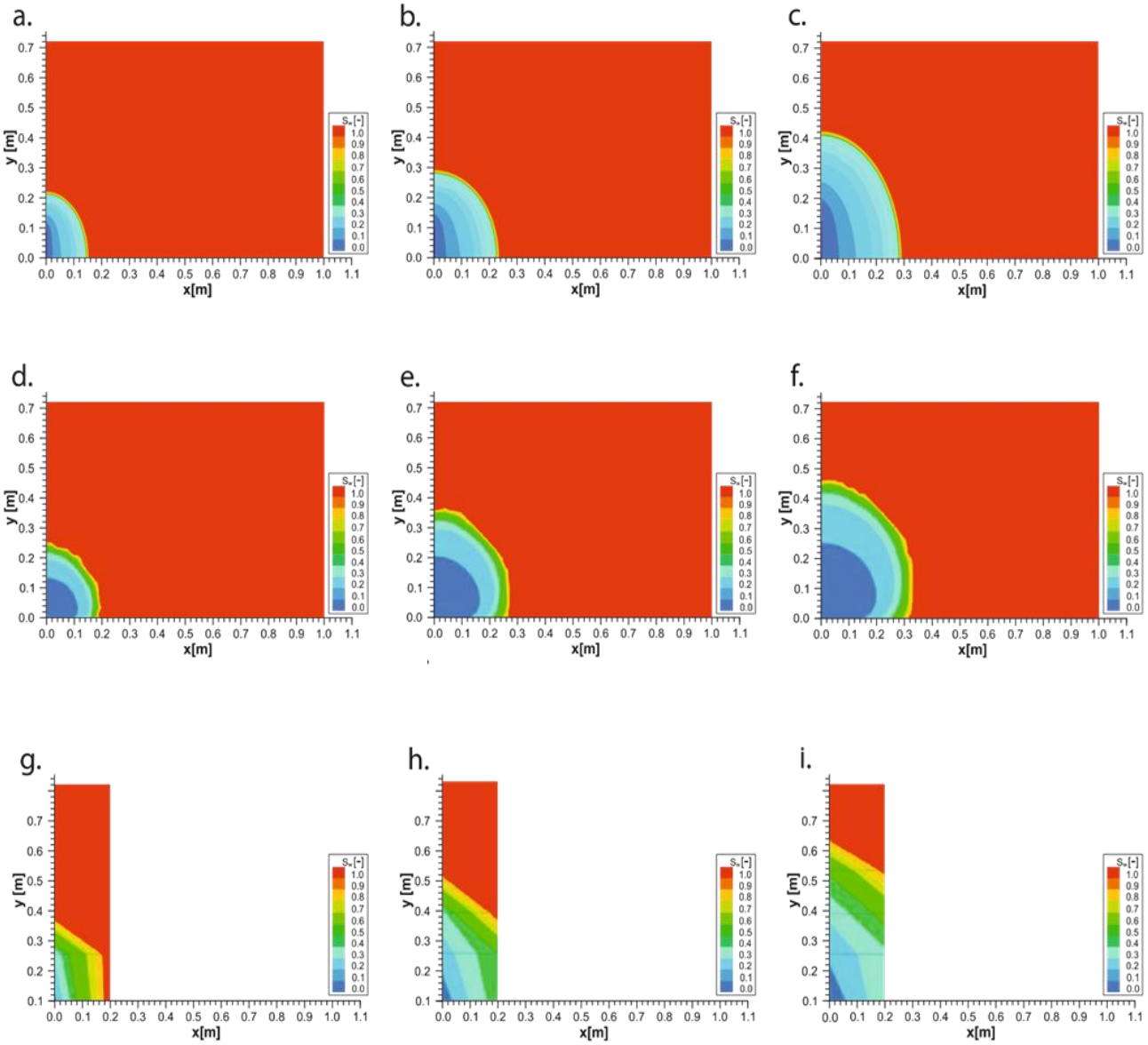

Fig. 5. Liquid-water saturation distribution during steam injection into the sandbox under soil water-saturated condition with the steam flow velocity of 3.6 kg/hr, over the processing times of 6, 12, and 18 min, for the case of; (a, b, c) simulation results of the DCC model in porous media. (d, e, f) numerical results of Darcy's law-based model, published in Ref. [17]. (g, h, i) experimental γ - density measurements, derived from Ref. [17]. "Reprinted with permission from Ref. [17]. Copyright 2010 by the American Geophysical Union."

temperature differences. Janfada et al. have explained the prediction method of heat losses based on the calculation of all sandbox serial and parallel resistances [6].

In spite of all mentioned physical reasons for the deviations, DCC simulation results are almost qualitatively similar to the experimental trends of the available paper results, containing colored map plots for steam injection into the sandbox under soil water-saturated condition, reported by *Ochs et al.* [17]. For providing a quantitative comparison, the propagated saturated temperature boundaries in the sandbox are extracted from the temperature sensor measurements and DCC model simulation outputs, using Figs. 6(a-c) and Figs. 6(g-i). The covered thermal areas, determined by the propagated saturated temperature fronts, are displayed in Fig. 7(a-c) for both experimental and DCC simulation results, over 6,

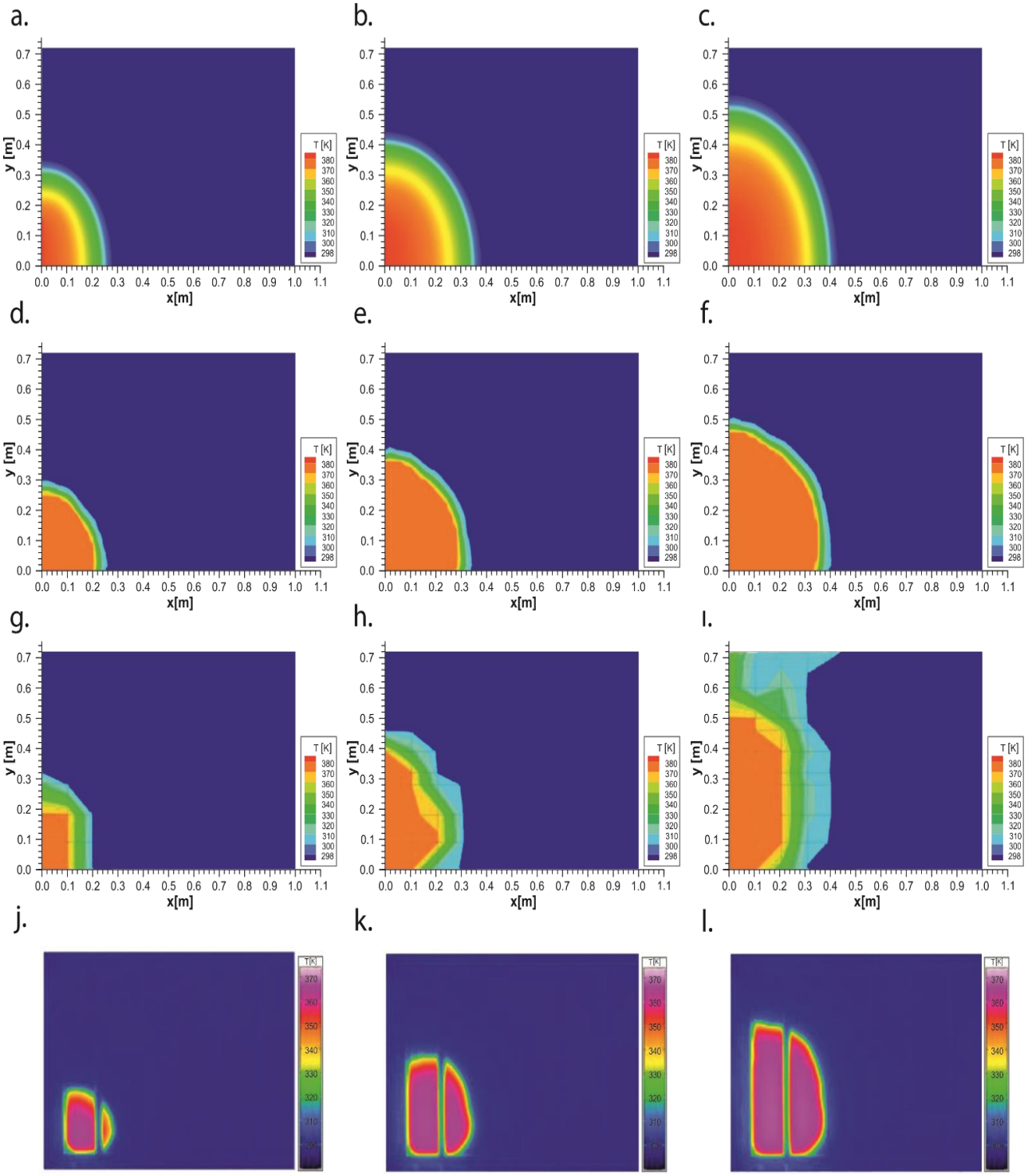

Fig. 6: Temperature distributions during steam injection into the sandbox under soil water-saturated conditions with the steam the flow velocity of 3.6 kg/hr, over the processing times of 6, 12, and 18 min, for the case of; (a, b, c) simulation results of the DCC model in porous media. (d, e, f) numerical results of Darcy's law-based model, published in Ref. [17]. (g, h, i) experimental Pt-100 sensors measurements, derived from Ref. [17]. (j, k, l) experimental thermographic camera measurements, derived from Ref. [17]. "Reprinted with permission from Ref. [17]. Copyright 2010 by the American Geophysical Union."

12, and 18 minutes after the beginning of the process. By counting the cells of the covered thermal areas in each graph paper, one may have access to the quantitative values of the covered thermal areas. The covered thermal areas values of the propagated thermal fronts in 6, 12, and 18 minutes after the beginning of the process are respectively 0.02, 0.059, and 0.098 m^2 for the experimental measurements, while corresponding covered areas of the simulation results are 0.025, 0.049, and 0.082 m^2 for the same mentioned times.

The absolute value of relative change percent (%) for experimental and simulation values of the covered thermal areas can be calculated by Eq. (46). The values of the covered thermal areas of the sandbox for the experimental measurements and DCC simulation results over the processing times of 6, 12, and 18 min are shown in Fig. 8.

$$\text{Relative change percent} = \left| \frac{A_E - A_S}{A_E} \right| \times 100 \quad (46)$$

in which, A_E and A_S are experimental and simulation values of the sandbox-covered thermal areas, extracted *via* propagated saturated temperature fronts over the processing time respectively.

Based on the calculated values of Table 2, in the sixth minute after the beginning of the process, the relative change percent between A_E and A_S is 25 %. As more process time elapses, the relative change percent roughly reduces to 16.3-16.9% within 12 and 18 minutes after the beginning of the process. This means, for the higher elapsed times, there is less difference between calculated percentages of relative change. In addition to the last main mentioned reasons for the available differences between Pt-100 sensors' temperature measurements and DCC simulation results, the higher relative change percent at the beginning of the process can be related to the initial transition status of the system. In other words, it can be the consequence of having less accuracy over the first minutes of the experimental process and more computational errors at the beginning of the simulation.

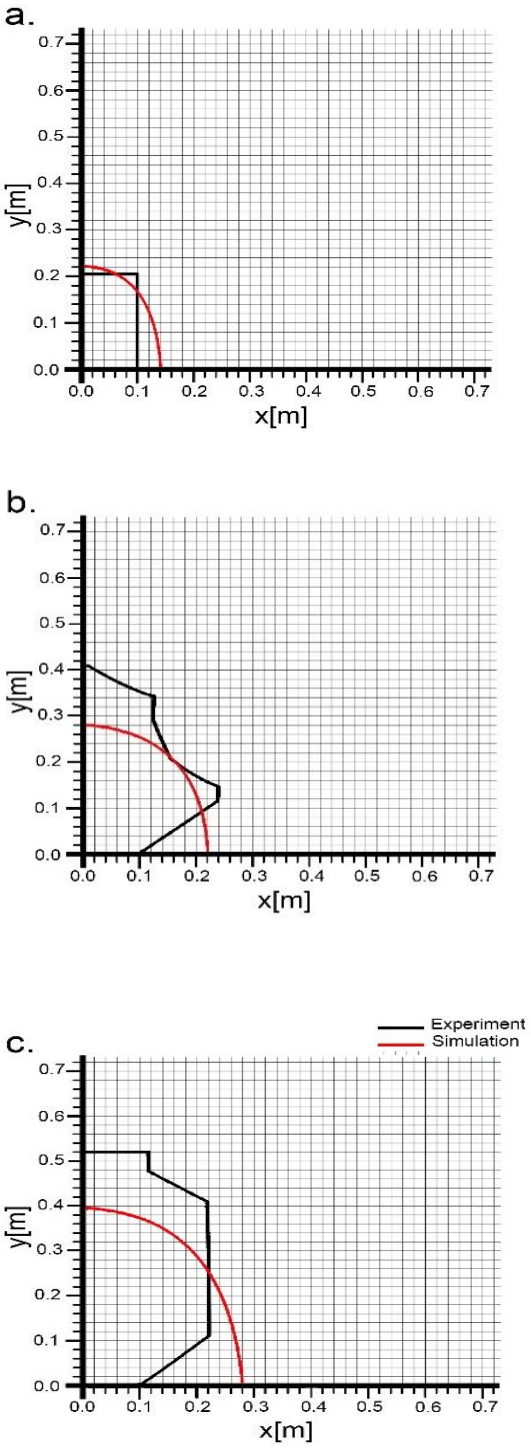

Fig. 7. Comparison between the covered thermal areas of the sandbox, extracted considering the propagated saturated temperature fronts over the processing times of 6, 12, and 18 min, for the experimental measurements (black line) and DCC simulation results (red line).

CONCLUSIONS

Using all steam advantages in a remediation process is only viable if steam arrives and covers all of the targeted contaminated areas. Therefore, the prediction of steam front propagation is required to demonstrate how steam can sweep the saturated zone of soil over time. In this

Table 2. Calculated absolute values of relative change percent (%) for the experimental and simulation values of the sandbox-covered thermal areas over the processing times of 6, 12, and 18 min.

Time (min)	Experimental covered area (m^2)	Simulation covered area (m^2)	The absolute value of relative change percent (%)
T	A_E	A_S	$\left\|(A_E - A_S)/A_E\right\| \times 100$
6	0.02	0.025	25
12	0.059	0.049	16.9
18	0.098	0.082	16.3

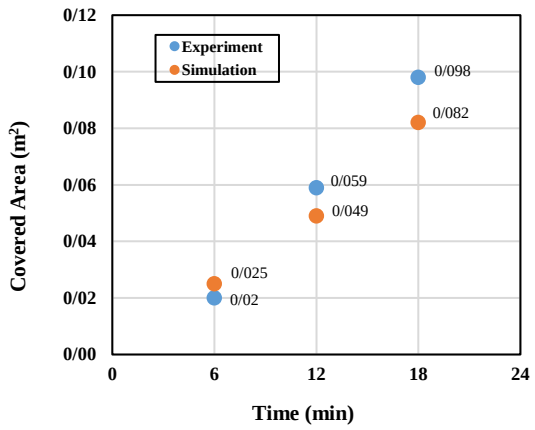

Fig. 8. Values of the covered thermal areas of the sandbox for the experimental measurements and DCC simulation results over the processing times of 6, 12, and 18 min.

the study, for the first time, the Direct Contact Condensation (DCC) model in porous media was developed for the numerical analysis and simulation of steam injection into the fully water-saturated zone of the soil to demonstrate how much this model can predict the spreading behavior and the shape of thermal fronts.

Considering the low residual saturation of the contaminant phase, and therefore, having a small effect of contamination on the steam propagation, it is possible to neglect the contaminant phase. Thus, only can take into consideration water and steam phases affecting steam propagation and thermal front boundary movement. The inclusion of the contaminant as a new component would enable the model to be used as a means of remediation study.

DDC model by considering thermal equilibrium only on the interfacial area is a two-resistance model. The interfacial area between two phases in each computational cell is considered under saturated conditions. In this model, each of the liquid and vapor phases takes into account individually in the process of heat transfer. Heat flux from the interface to the liquid phase is set equal to heat flux from the vapor phase to the interface leading to the calculation of the condensation rate. Then, in the Eulerian multiphase flow model, the mass and enthalpy source terms due to the calculated condensation rates were added to the continuity and enthalpy equations of the liquid phase. Pressure drop due to flowing fluids in the porous structure was considered by lumped approach model using viscous and inertial loss terms added to momentum equations. The present model was validated by comparison with the latest available published experimental data. The comparison has demonstrated fair agreement for temperature and saturation distribution over time. The spreading behavior and the shape of the fronts were reproduced with the DCC model, although the simulation results show some deviations from the experimental measurements, which can be the consequence of the mentioned physical reasons for the available experimental results. This may be listed as follows:

- Possible presence of non-condensable gases along with used steam in the experimental process.
- Restriction of sequential procedure for the experimental γ density-based saturation measurements.
- Experimental inaccuracies due to Pt-100 temperature sensors arranged at a ten-centimeter distance from each other and therefore linear interpolation of measurements.
- Having higher heat losses due to removing insulation to take photos with the thermographic camera.
- More heat losses, around sandbox steel framework and metal beams regarding higher thermal conductivities of the metal.

The mentioned reasons related to heat losses are not available and are thus effective in the process of steam injection at real contaminated sites. In addition, the simulation

of steam injection into the sandbox is very complex and needs some simplifications to make it affordable in terms of computational cost. In order to simplify and reduce computational costs, heat losses were considered as a sink term based on the calculated overall heat transfer coefficient and local temperature differences. The overall heat transfer coefficient has been predicted according to the calculation of all available sandbox serial and parallel resistances [6].

The covered thermal areas of the sandbox, extracted from propagated saturated temperature fronts, were compared quantitatively for the experiments and simulation results of the DCC model over 6, 12, and 18 min after the beginning of the process. The corresponding covered area values were respectively 0.02, 0.059, and 0.098 m^2 for the experiment and 0.025, 0.049, and 0.082 m^2 for the simulation. Then absolute values of the relative change percent of the covered thermal areas have been evaluated for the experimental and simulation. After 6 minutes from the beginning of the process, the absolute value of the relative change is 25%. After elapsing 12 and 18 minutes from the beginning of the process, the evaluated percentages of the relative change are within 16.3% and 16.9%. It can be stated that the higher percentage of the relative change at the beginning of the process could be related to the consequence of having less accuracy in the first minutes of the experimental process and more computational errors at the beginning of the simulation.

Nomenclatures

A_i	Interfacial area, m^2
A_{lg}	Interfacial area per unit volume, m^{-1}
A_E	Sandbox covered thermal area extracted from experimental measurements, m^2
A_S	Sandbox covered thermal area extracted from DCC simulation results, m^2
a	Forchheimer constant
C_i	Inertial resistance parameter of phase i
C_E	Ergun constant
c_{pm}	Specific heat capacity of soil, kJ/(kg.K)
d_g	Bubble diameter of the gas phase, m
d_p	Bubble diameter of the p^{th} phase, m
d_m	Mean bed particle diameter, m
$F_{lift,q}$	Lift force, $kg.m/s^2$
F_q	External body force including buoyancy, $kg.m/s^2$
$F_{vm,q}$	Virtual mass force, $kg.m/s^2$
h_q	Specific enthalpy of the q^{th} phase (total energy of a unit mass), kJ/kg
h_l	Heat transfer coefficient of the liquid phase, W/(m.K)
h_g	Heat transfer coefficient of vapor phase, $W/(m^2.K)$
H_l	Volumetric heat transfer coefficient of liquid phase, $W/(m^3.K)$
H_g	Volumetric heat transfer coefficient of vapor phase, $W/(m^3.K)$
H_{ls}	Saturation enthalpy of the liquid phase, J/kg
H_{gs}	Saturation enthalpy of vapor phase, J/kg
H_{pq}	Interphase enthalpy, J/kg
ΔH	Latent heat of evaporation, J/kg
K	Hydraulic conductivity, m/s
k_{cond-q}	Thermal conductivity coefficient of the q^{th} phase, W/(m.K)
k_s	Thermal conductivity of dry soil, W/(m.K)
k	Absolute permeability, m^2
k_i	Effective permeability of the i^{th} phase, m^2
k_{ri}	Relative permeability of the i^{th} phase, [ ]
$\dot{m}_{gas-int}$	Rate of mass transfer from the gas phase to interface per unit of area, $kg/(s.m^2)$
$\dot{m}_{int-liq}$	Rate of mass transfer from interface to the liquid phase per unit of area, $kg/(s.m^2)$
n	Van Genuchten parameter, [ ]
Nu_p	Nusselt number of the p^{th} phase, [ ]
P	Distributed pressure for all phases, $kg/(m.s^2)$
q_l	Liquid phase convective heat transfer per unit of area, $W\cdot m^{-2}$
q_g	Steam phase convective heat transfer per unit of area, $W\cdot m^{-2}$
$Q_{int-liq}$	Heat transfer from interfacial area to liquid phase per unit of area, $W\cdot m^{-2}$
$Q_{gas-int}$	Heat transfer from vapor to interfacial area per unit of area, $W\cdot m^{-2}$
R_{pq}	Interaction force between phases, $kg.m/s^2$
S_q	Source/sink terms
S_{we}	Effective saturation of wetting phase, [ ]
S_{ne}	Effective saturation of non-wetting phase, [ ]
S_{wr}	Residual saturation of wetting phase, [ ]
S_{nr}	Residual saturation of non-wetting phase, [ ]
u_q	q^{th} phase velocity, m/s
u_{pq} (u_{qp})	Interphase velocities, m/s
V	Total volume, m^3
V_q	Volume of the q^{th} phase, m^3
T	Temperature, K

T_s	Saturation temperature, K
T_{int}	Interfacial temperature, K
∇p	Pressure drop, kg/(m.s^2)

Greek Letters

α_i	Volume fraction of the ith phase
α_{VG}	Van Genuchten parameter, Pa^{-1}
ε	Porosity, [ ]
μ	Viscosity, kg/(m.s)
ρ	Density, kg/m^3
ρ_{sg}	Soil grain density, kg/m^3
τ	Shear stress, kg/(m.s^2)

Indexes

g	Gas phase
l	Liquid phase
I	ith phase
p	pth phase
q	qth phase
n	Non-wetting phase
w	Wetting phase

Acknowledgments

The authors wish to thank Holger Class, professor at the Dept. of Hydromechanics and Modeling of Hydrosystems, Stuttgart University, for our fruitful and constructive discussions about non-isothermal multiphase flow in porous media.

Received : Sep. 21, 2021 ; Accepted : Nov. 29, 2021

REFERENCES

[1] Tirandaz H., Shaeyan M., Ghanbarpour S., Seyedipour N.A., Khodaverdi H., Dastgheib S.M.M., The Succession of Dominant Culturable Hydrocarbon-Utilizing Bacteria During Bioremediation of Oil-Based Drilling Waste, *Iran. J. Chem. Chem. Eng. (IJCCE)*, **38**: 267–277 (2019).

[2] Koteswara R.G., Kiran Y., Vijaya L.U., Reducing Agents Enhanced Electrokinetic Soil Remediation (EKSR) for Heavy Metal Contaminated Soil, *Iran. J. Chem. Chem. Eng. (IJCCE)*, **38**: 183–199 (2019).

[3] Arbabi M., Nasseri S., Chimezie A., Biodegradation of Polycyclic Aromatic Hydrocarbons (PAHs) in Petroleum Contaminated Soils, *Iran. J. Chem. Chem. Eng. (IJCCE)*, **28(3)**: 53-59 (2009).

[4] Shirdam R., Daryabeigi Zand A., Nabi Bidhendi G., Mehrdadi N., Removal of Total Petroleum Hydrocarbons (TPHs) from Oil-Polluted Soil in Iran, *Iran. J. Chem. Chem. Eng. (IJCCE)*, **28**: 105–113, (2009).

[5] Ezzatian R., Voussoughi M., Yaghmaei S., Abedi Koupai J., Borghaei M., Azuki G.R., Abedi Koupai J., Borghaei M., Pazuki G.R., Effect of C/N Ratio on the Phytoremediation of Crude Oil Contaminated Soils by Puccinellia Distance, *Iran. J. Chem. Chem. Eng. (IJCCE)*, **27**: 77–85 (2008).

[6] Janfada T.S., Class H., Kasiri N., Dehghani M.R., Comparative Experimental Study on Heat-up Efficiencies During Injection of Superheated and Saturated Steam into Unsaturated Soil, *Int. J. Heat Mass Transf.*, **158**: 119235 (2020).

[7] Ochs S.O., Steam Injection into Saturated Porous Media–Process Analysis Including Experimental and Numerical Investigations, (2006).

[8] Smith J.M., Van Ness H.C., Abbott M.M., "Introduction to Chemical Engineering Thermodynamics", 7th ed. McGraw-Hill, (2004).

[9] Class H., "Models for Non-Isothermal Compositional Gas-Liquid Flow and Transport in Porous Media", Habilitationsschrift, Stuttgart University (2007).

[10] Kleinknecht S.M., "Steam Injection Technique for In Situ Remediation of Chlorinated Hydrocarbons from Low Permeable Saturated Zones-Experiment and Numerical Approach", M.Sc. Thesis, Stuttgart University (2011).

[11] Emert M., "Numerische Modellierung Nichtisothermer Gas-Wasser Systeme in Porösen Medien (Numerical Modelling of Non-Isothermal Gas-Water Systems in Porous Media", Ph.D. Thesis, Inst. Model. Hydraul. Environ. Syst. Stuttgart University (1997).

[12] Helmig R., Class H., Färber A., Emmert M., Heat Transport in the Unsaturated Zone – Comparison of Experimental Results and Numerical Simulations, *J. Hydraul. Res.* **36**: 933–962 (1998).

[13] Class H., Helmig R., Bastian P., Numerical Simulation of Non-isothermal Multiphase Multicomponent Processes in Porous Media. 1. An Efficient Solution Technique, *Adv. Water Resour.*, **25**: 533–550 (2002).

[14] Class H., Helmig R., Numerical Simulation of Non-Isothermal Multiphase Multicomponent Processes in Porous Media. 2. Applications for the Injection of Steam and Air, *Adv. Water Resour.*, **25**: 551–564, (2002).
[15] Schmidt R., Gudbjerg J., Sonnenborg T.O., Jensen K.H., Removal of NAPLs from the Unsaturated Zone Using Steam: Prevention of Downward Migration by Injecting Mixtures of Steam and Air, *J. Contam. Hydrol.*, **55**: 233–260 (2002).
[16] Gudbjerg J., "Remediation by Steam Injection", Ph.D. Thesis, Environment and Resources DTU, Technical University of Denmark (2003).
[17] Ochs S.O., Class H., Färber A., Helmig R., Methods for Predicting the Spreading of Steam below the Water Table During Subsurface Remediation, *Water Resour. Res.*, **46**: (2010).
[18] Dhir V.K., Condensation, *Access Sci.* (2014).
[19] Babanezhad M., Nakhjiri A.T., Rezakazemi M., Shirazian S., Developing Intelligent Algorithm as a Machine Learning Overview over the Big Data Generated by Euler–Euler Method to Simulate Bubble Column Reactor Hydrodynamics, *ACS Omega.*, **5**: 20558–20566, (2020).
[20] Rezakazemi M., Shirazian S., Development of a 3D Hybrid Intelligent-Mechanistic Model for Simulation of Multiphase Chemical Reactors, *Chem. Eng. Technol.*, **41**: 1982–1993 (2018).
[21] FLUENT 13 Documentation, Fluent Inc., (2013).
[22] ANSYS Help 18.2, *ANSYS Inc.*, (2018).
[23] Ranade V.V., "Computational Flow Modeling of Chemical Reactor Engineering", Academic Press, (2002).
[24] Ranz W.E., Marshall W.R., Evaporation from Drops, Part I, and Part II, *Chem. Eng. Prog*, **48**: 173–180 (1952).
[25] Shah A., Chughtai I.R., Inayat M.H., Numerical Simulation of Direct-contact Condensation from a Supersonic Steam Jet in Subcooled Water, *Chinese J. Chem. Eng.*, **18**: 577–587 (2010).
[26] Shah A., Chughtai I.R., Inayat M.H., Experimental and Numerical Analysis of Steam Jet Pump, *Int. J. Multiph. Flow.*, **37**: 1305–1314 (2011).
[27] Tortike S.M., Farouq Ali W.S., "Saturated Steam Property Functional Correlations for Fully Implicit Thermal Reservoir Simulation", *SPE*, University of Alberta (1989).
[28] Brucker G.G., Sparrow E.M., Direct Contact Condensation of Steam Bubbles in Water at High Pressure, *Int. J. Heat Mass Transf.*, **20**: 371–381 (1977).
[29] Ahmed T., "Reservoir Engineering Handbook", 5th ed., Gulf Professional Publishing (2019).
[30] Bastian P., "Numerical Computation of Multiphase Flows in Porous Media", Habilitationsschrift, Kiel University (1999).
[31] Jambhekar V.A., "Forchheimer Porous-media Flow Models - Numerical Investigation and Comparison with Experimental Data", M.Sc. Thesis, Stuttgart University (2011).